World Academy of Science, Engineering and Technology
International Journal of Mechanical and Mechatronics Engineering
Vol:9, No:5, 2015

Simulation Studies of Solid-Particle and Liquid-Drop Erosion of NiAl Alloy

Rong Liu, Kuiying Chen, Ju Chen, Jingrong Zhao, Ming Liang

***Abstract*—**This article presents modeling studies of NiAl alloy under solid-particle erosion and liquid-drop erosion. In the solid-particle erosion simulation, attention is paid to the oxide scale thickness variation on the alloy in high-temperature erosion environments. The erosion damage is assumed to be deformation wear and cutting wear mechanisms, incorporating the influence of the oxide scale on the eroded surface; thus the instantaneous oxide thickness is the result of synergetic effect of erosion and oxidation. For liquid-drop erosion, special interest is in investigating the effects of drop velocity and drop size on the damage of the target surface. The models of impact stress wave, mean depth of penetration, and maximum depth of erosion rate (Max DER) are employed to develop various maps for NiAl alloy, including target thickness vs. drop size (diameter), rate of mean depth of penetration (MDRP) vs. drop impact velocity, and damage threshold velocity (DTV) vs. drop size.

***Keywords*—**Liquid-drop erosion, NiAl alloy, oxide scale thickness, solid-particle erosion.

I. Introduction

SOLID-particle erosion and liquid-drop erosion both are popular wear modes that cause serious problems in many engineering systems, including steam and jet turbines, pipelines and valves carrying particulate matter, and fluidized bed combustion systems. Solid-particle erosion is caused by the impingement of small, solid particles against a surface, resulting in the loss of the material [1]. Liquid-drop erosion can be described as the collision at high speed of liquid droplets with a solid surface, which causes the removal of material from the surface [2]. Although experimental investigation prevails in erosion research, due to high capital cost and long duration of erosion tests, various simulation models have been developed, including physics-based and statistics-based erosion models, to predict/reveal the erosion resistance/mechanisms of materials. One of the most popular models was developed based on an ideal ductile, non-work hardening solid material eroded by rigid particles [3]. Another model was created for single-particle erosion of metals that assumed that material cutting and material deformation occurred simultaneously but further suggested that "deformation wear" governed at normal impact while "cutting wear" prevailed at acute angles [4]-[6].

Erosion of metallic materials at high temperatures is influenced by oxidation. Erosion-oxidation maps are very useful in high-temperature erosion study because they are a means by which the change in erosion-corrosion mechanism – ranging from the erosion of the substrate to the erosion of the corrosion product – is given as a function of an erosion and corrosion parameter [7]. Several physics-based models have been developed, which describe the interaction between erosion and oxidation [8]-[11]. According to the thickness of the oxide on the eroded surface, three boundaries were defined as at the first boundary the protection provided by the oxide scale was negligible and the substrate surface took most of the impact energy when the oxide film was thin; at the second boundary the oxide was able to take all the plastic deformation and therefore there was no any plastic deformation taking place in the substrate because the oxide scale thickness reached the same level as the plastic deformation zone; and at the third boundary the impact from particles was all absorbed by the oxide scale and no plastic deformation occurred in the substrate region [10].

The earliest model of liquid impingement erosion was established to investigate the deformation of the solid target material in the initial stage of damage [12], which proposed that at the moment of initial impingement, a stress wave generated immediately traveled back from solid-liquid contact into liquid and the liquid exhibited compressible behavior. This model was improved, suggesting that high pressure occurred in liquid impingement erosion and expressed the impact pressure as a function of the density of the liquid, the compressibility of the liquid and the impact velocity of liquid droplet [13], and the pressure equation was modified with the impact of spherical drop and consideration of the elastic deformation of the liquid drop [14]. In order to predict the response of a material in liquid impingement erosion, scientists attempted to find the relationships between erosion resistance and mechanical properties of materials such as hardness, tensile strength, fracture toughness and strain energy. The measurements of erosion resistance of materials can fall into the main aspects such as maximum rate of weight loss, mean depth of penetration, rationalized erosion rate and maximum depth of erosion rate (Max DER) [15]-[21].

In this research, the resistance of NiAl alloy, which is a widely used alloy in erosion environments, to solid-particle erosion and liquid-drop erosion was investigated through analytically modeling. An analytical model was created that can predict the oxide scale thickness at a given time interval for steels and alloys under high-temperature erosion at a set particle impact velocity and impinging angle, based on the four-regime classification of eroded surface [9] and the formulation of oxide growth rate [22], utilizing deformation

Rong Liu is with Carleton University, Ottawa, Ontario, K1S 5B6 Canada (phone: 613-5202600; fax: 613-5205715; e-mail: Rong.Liu@carleton.ca).

Kuiying Chen is with National Research Council Canada, Ottawa, Ontario, K1A 0R6 Canada (e-mail: Kuiying.Chen@nrc-cnrc.gc.ca).

Ju Chen, Jingrong Zhao, and Ming Liang are with University of Ottawa, Ottawa, Ontario, K1N 6N5 Canada (e-mail: juchen2011@hotmail.com, zjrstacie@hotmail.com, Ming.Liang@uOttawa.ca).

wear and cutting wear mechanisms of materials in erosion [6]. The obtained results from the model were plotted to show the oxide thickness variation with erosion time of NiAl alloy under different temperatures and erosion conditions such as particle impact velocity and particle impinging angle. For liquid impingement erosion analytical models of impact stress wave, mean depth of penetration, and Max DER were employed. The liquid impingement erosion resistance of NiAl alloy was characterized by establishing the relationships between target thickness and drop size (diameter), between rate of mean depth of penetration (MDRP) and drop impact velocity, and between damage threshold velocity (DTV) and drop size.

II. Solid-Particle Erosion Modeling

A. Formulation of Oxidation

Oxidation process controls the oxide growth on a metal surface in high-temperature environments. Kang et al. [9] defined the rate of oxide scale growth in high-temperature erosion using:

$$\frac{dX}{dt} = \frac{K_{ce}}{X} - K, \tag{1}$$

where K_{ce} is the parabolic rate of oxide growth, which is a function of the target metal composition, the corrosive condition and the erosive condition; K is the erosion rate of corrosion product (oxide), which is a function of the type of corrosion product and the erosive condition. To compute the oxide scale growth rate, the value of K_{ce} must be obtained as an initial input. With the input value of temperature T, the relationship between the parabolic constant of oxide growth K_p and K_{ce} is given as [22]

$$K_p = K_{ce}\left(\frac{bM_o}{aV_m}\right)^2, \tag{2}$$

where, for an oxide M_aO_b a and b are the numbers in the description, M_o is the atomic weight of oxygen, and V_m is the molar volume of the target metal. Rearranging (2) gives:

$$K_{ce} = K_p\left(\frac{aV_m}{bM_o}\right)^2. \tag{3}$$

B. Formulation of Erosion

In high-temperature erosion, the oxide thickness on the metal target surface is reduced by erosion. To obtain the oxide thickness reduction rate, the erosion mechanisms at high temperatures should be clearly identified. Bitter [5] devised a method to describe erosion based on energy conservation. It was assumed that the total erosion energy W_e was constant for two types of erosion, deformation erosion (W_D) and cutting erosion (W_{C1} and W_{C2}). In detail, the total erosion energy can be expressed as [5]

$$W_e = W_D + W_{C1}, \text{ if } \alpha \le \alpha_0, \tag{4}$$

$$W_e = W_D + W_{C2}, \text{ if } \alpha \ge \alpha_0, \tag{5}$$

where α is the incident particle angle impacting on the target material. α_0 is the impact angle at which the horizontal velocity equals zero when the particle leaves the surface. The deformation erosion energy is given as [5]

$$W_D = \frac{\frac{1}{2}M\left(V\sin\alpha - K_1\right)^2}{\delta}, \tag{6}$$

and the cutting erosion energy is expressed as [5]

$$W_{C1} = \frac{2MC\left(V\sin\alpha - K_1\right)^2}{\sqrt{V\sin\alpha}}\left[V\cos\alpha - \frac{C\left(V\sin\alpha - K_1\right)^2}{\sqrt{V\sin\alpha}}\chi\right], \tag{7}$$

$$W_{C2} = \frac{\frac{1}{2}M\left[V^2\cos^2\alpha - K_2\left(V\sin\alpha - K_1\right)^{3/2}\right]}{\chi}. \tag{8}$$

The parameters in (7) and (8) are given as [5]

$$C = \frac{0.288}{y}\sqrt[4]{\frac{d}{y}}, \tag{9}$$

$$K_1 = \frac{\pi^2}{2\sqrt{10}}y^{5/2}\left(\frac{1}{d}\right)^{1/2}\left(\frac{1-q_1^2}{E_1} + \frac{1-q_2^2}{E_2}\right)^2, \tag{10}$$

$$K_2 = 0.82y^2\sqrt[4]{\frac{y}{d}}\left(\frac{1-q_1^2}{E_1} + \frac{1-q_2^2}{E_2}\right)^2, \tag{11}$$

where d is the density of particle; E_1, E_2, q_1 and q_2 are the Young's modulus and Poisson's ratio of particle and target material, respectively; δ is deformation wear factor; χ is cutting wear factor; M is the total mass of impinging particles; V is particle impact velocity; y is elastic load limit.

The erosion theory given by [5] shows complex forms in terms of expression and implementation, which were concerned by [6] to seek a simpler analytical solution. The new solutions could readily correlate experimental data. The simplified erosion model for erosion loss in weight takes the following form

$$W = \frac{\frac{1}{2}MV^2\cos^2\alpha\sin n\alpha}{\phi} + \frac{\frac{1}{2}M\left(V\sin\alpha - \kappa\right)^2}{\varepsilon}, \text{ if } \alpha \le \alpha_0, \tag{12}$$

and

$$W = \frac{\frac{1}{2}MV^2\cos^2\alpha}{\phi} + \frac{\frac{1}{2}M\left(V\sin\alpha - \kappa\right)^2}{\varepsilon}, \text{ if } \alpha > \alpha_0, \tag{13}$$

where κ is the velocity component normal to the surface below which no erosion takes place in certain hard materials; ϕ and ε are cutting and deformation wear factors, respectively; n is a constant. In order to obtain the thickness reduction rate of the oxide scale, the total mass of impact particles M in (12) and (13) was changed to m/d, where m is particle mass per unit area per second and d is the density of particle. This gives the erosion loss in thickness as

$$L=\frac{\frac{1}{2}mV^2\cos^2\alpha\sin n\alpha}{\phi d}+\frac{\frac{1}{2}m(V\sin\alpha-\kappa)^2}{\varepsilon d},\ \text{if}\ \alpha\le\alpha_0, \tag{14}$$

and

$$L=\frac{\frac{1}{2}mV^2\cos^2\alpha}{\phi d}+\frac{\frac{1}{2}m(V\sin\alpha-\kappa)^2}{\varepsilon d},\ \text{if}\ \alpha>\alpha_0. \tag{15}$$

C. Growth Rate of Oxide Scale

The above analysis procedure includes two aspects: increase in oxide scale thickness due to oxidation and reduction of oxide scale thickness because of erosion attack. From the above analyses, the instantaneous scale thickness change rate can be obtained. Consider (1) again, combining (3), (14) and (15), the change rate of oxide scale thickness is expressed as

$$\frac{dX}{dt}=\frac{K_P\left(\frac{aV_m}{bM_o}\right)^2}{X}-\left[\frac{\frac{1}{2}mV^2\cos^2\alpha\sin n\alpha}{\phi d}+\frac{\frac{1}{2}m(V\sin\alpha-\kappa)^2}{\varepsilon d}\right],$$
$$\text{if}\ \alpha\le\alpha_0, \tag{16}$$

and

$$\frac{dX}{dt}=\frac{K_P\left(\frac{aV_m}{bM_o}\right)^2}{X}-\left[\frac{\frac{1}{2}mV^2\cos^2\alpha}{\phi d}+\frac{\frac{1}{2}m(V\sin\alpha-\kappa)^2}{\varepsilon d}\right],$$
$$\text{if}\ \alpha>\alpha_0. \tag{17}$$

To solve the above differential equations, the value of parabolic constant of oxide growth K_p must be known. It can be obtained experimentally according to the equation [10]:

$$K_P=\frac{[\rho X(1-f)]^2}{t}, \tag{18}$$

where ρ is the density of oxide scale; f is the stoichiometric factor that accounts for the percentage of the metal consumed in the formation of oxide; and t is the time of exposure. Thus, once the parameters in (16) and (17) are defined, the differential equations can be solved and the variation of the oxide thickness with erosion time for a given particle impact velocity and impinging angle can be obtained. Based on the variation of the oxide thickness, the erosion behavior can be predicted with respect to the four-regime of eroded surface [9]. Regime 1 — erosion of metal may not occur unless the metal is non-oxidable. If the oxide thickness decreases with erosion time, the oxide scale will be totally removed from the eroded surface after a certain period of time and eventually the substrate material will be subjected to erosion. In this case, regime 2 — oxidation-affected erosion predominates. On the contrary, if the oxide growth rate in erosion process is greater than the oxide growth rate without erosion process involved, oxidation will benefit the erosion resistance of the substrate material; then regime 3 — erosion-enhanced oxidation takes place. Finally, as the growth rate of the oxide is high enough to avoid the particles reaching the substrate surface, erosion can only occur in the oxide scale. This erosion falls into regime 4 — oxide erosion.

III. Liquid-Drop Erosion Modeling

A. Impact Stress Wave

In the liquid impingement erosion theories given by [12]-[14]; it was suggested that at the moment of initial impingement, a stress wave generated immediately traveled back from solid-liquid contact into liquid at a certain velocity and the liquid exhibited compressible behavior. High pressure occurred in liquid impingement erosion due to water-hammer effect and the impact pressure can be expressed as functions of liquid properties and drop normal impact velocity (V_0). Heymann [23] deemed that in consideration of droplet impacting at 90 degree on a smooth and rigid surface, the impact stress reached the maximum (peak) near the contact area, however, at the exact contact point it remained a relatively small (bottom) value due to the release of the waves that generated the pressure distribution map. This high pressure led to the occurrence of ring cracks and fractures in the area within radius r_0 in the top surface layer of the target, as schematically shown in Fig. 1.

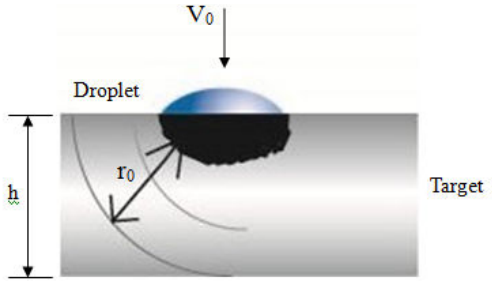

Fig. 1 Ring cracks induced in the top surface layer of the target attacked by liquid drop

The radius r_0 is expressed as [2]

$$r_0=\frac{2h}{\left[(c_d/c_R)^2-1\right]^{1/2}}, \tag{19}$$

where h is the thickness of target, see Fig. 1, c_d and c_R are the dilatational velocity and Rayleigh wave velocity, respectively. Considering the inherent elasticity of the material, the velocity of Rayleigh wave is generally thought to be equal to that of shear wave, and then can be calculated as [24]

$$c_R=\sqrt{\frac{G}{\rho}}, \tag{20}$$

where G and ρ are the shear modulus and density of target material, respectively. The occurrence of erosion damage on target surface depends on the duration of drop incidence time and the duration of the stress wave. When the former is longer

than the latter, erosion damage occurs [2], i.e., $\frac{2d}{c_L} > \frac{h}{c_S}$. Therefore, to avoid erosion damage, the minimum target thickness can be determined by

$$h = \frac{2dc_s}{c_L}, \tag{21}$$

where d is the size (diameter) of liquid drop, c_L and c_S are sound speeds of liquid and solid, respectively, can be calculated by [25], [26]

$$c_L = \sqrt{\frac{\kappa_0}{\rho_0}}, \tag{22}$$

$$c_S = \sqrt{\frac{E}{\rho}}, \tag{23}$$

where κ_0 is the bulk modulus of liquid drop and E is the Young's modulus of solid target; ρ_0 and ρ are the densities of liquid drop and solid target, respectively. From (21) it is evident that for a given target material the minimum thickness h for preventing erosion damage from occurring is solely proportional to the drop size for erosion damage occurring.

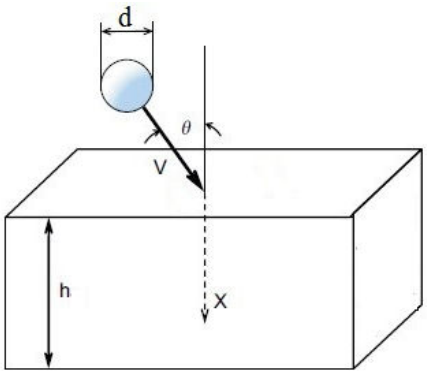

Fig. 2 Incoming liquid drop on solid surface at an incident angle θ [27]

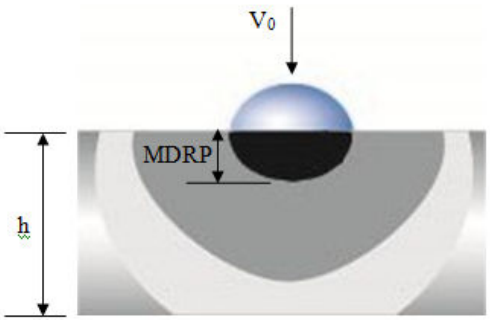

Fig. 3 Mean depth of penetration of liquid drop into solid surface

B. Mean Depth of Penetration

When a liquid droplet having a diameter d impacts a solid surface at an inclined angle θ with a velocity V, as illustrated in Fig. 2 [27]; [15] described the rate of mean depth of penetration (MDRP), as shown in Fig. 3, by the following equations, which is the change rate of an average thickness of the surface subjected to liquid impact erosion.

$$MDRP' = \left(\frac{\eta}{\varepsilon}\right)\left(\frac{A_p}{F}\right)\left(\frac{\rho_0 V_0^3}{2}\right), \tag{24}$$

$$MDRP = \left(\frac{\eta}{\varepsilon}\right)\left(\frac{A_p}{F}\right)\left(\frac{\rho_0 V_0^3}{2}\right)F, \tag{25}$$

where η is the efficiency of energy transfer between the liquid and solid, ε is the energy to remove unit volume of the target material, V_0 is the critical velocity for normal drop impact at which erosion occurs, F and A_p are exposed target area and projected target area, respectively. According to Fig. 2 [27],

$$V = V_0 / \cos\theta \tag{26}$$

The volume of eroded surface layer (ΔV) related to the energy (ε) absorbed by eroded material is given as

$$\varepsilon = \Delta V \cdot S_c = F \cdot h \cdot S_c, \tag{27}$$

where S_c is the erosion strength parameter that can be determined by a computational procedure based on experimental measurements.

To be more general, [16] proposed an expression of erosion rate (E_r) with the incident angle,

$$E_r \propto \frac{(V - V\cos\theta - V_c)^n}{\cos\theta}, \tag{28}$$

where V_c denotes the velocity below the critical value of no mass loss, $n \in [5,13]$ is a constant and depends on the target material properties. When $\theta = 0$, $V = V_0$, in this case, it is assumed that $\eta = 1$ and $F = A_p$. Substituting (21) into (27) gives

$$\varepsilon = F \cdot \frac{2dc_S}{c_L} \cdot S_c \tag{29}$$

Combining (22), (23), (25) and (29) yields

$$MDRP = \frac{\rho_0 \cdot V_0^3 \sqrt{\frac{\kappa_0}{\rho_0}}}{4d \cdot S_c \sqrt{\frac{E}{\rho}}} \tag{30}$$

C. Maximum Depth of Erosion Rate

Hattori [17] compared maximum depth of erosion rate (Max DER) of different materials, correlating Max DER with exposure time. Three time intervals can be identified in the Max DER-*t* map: incubation, acceleration, and maximum rate stages. The duration time of incubation depends on the impact velocity. The exponent of erosion rate is given on the basis of the volume

of the liquid impinging per unit time and is also certainly proportional to impact velocity. Thus impact velocity is a key parameter to be investigated, especially threshold velocity at the moment when erosion rate is zero or negligible.

In terms of threshold velocity, [18] and [19] defined pathbreaking damage threshold velocity (DTV) as the lower impact velocity at which damage occurred. The material's erosion resistance was widely characterized by absolute damage threshold velocity (ADTV). Hand and Field [20] proposed a linear relationship between ADTV and log of the fracture toughness of target material for 2 mm diameter water drops. They attempted to minimize the number of impacts and to decrease the velocity in order to get the threshold value. Evans et al. [21] defined a theoretical expression for DTV given by

$$DTV = 1.41\left(\frac{K_{IC}^{\ 2} c_R}{\rho_0^{\ 2} c_w^{\ 2} d}\right)^{1/3}, \tag{31}$$

where K_{IC} is the fracture toughness of target material, C_w is compressive wave velocity, which is related to material properties [24]

$$c_w = \sqrt{\frac{\kappa + \frac{4}{3}G}{\rho}}, \tag{32}$$

where G and κ are the shear modulus and bulk modulus of solid target, respectively. The value of DTV is beneficial for controlling the impact velocity, predicting the exact timing of damage occurrence and avoiding the damage.

IV. Erosion of Aluminum-Nickel Alloy

A. Parameters in Models for NiAl Alloy

The NiAl alloy investigated in this research is CMSX-4; its chemical composition is given in Table I. The oxidation behavior of Ni-Al alloy has been investigated by [28], showing that two alumina phases (θ-Al_2O_3 and α-Al_2O_3) are present in the oxide product. The values of the parabolic rate constant K_p were calculated from the experimental measurements of the oxide geometry at different temperatures, and also using other parameters, according to (18); these values are reported in Table II [28].

TABLE I
Chemical Composition of CMSX-4 Alloy

Ni	Cr	Co	Al	W	Mo	Ta	Hf	Re
61.8	6.5	9	5.6	6	0.6	6.5	1	3

TABLE II
Parabolic Oxidation Rate Constants of CMSX-4 Alloy

Temperature (°C)	K_p (kg^2/m^4·h)
850	9.76E-9
900	2.04E-8
950	2.61E-8

In the differential equations (16) and (17), cutting and deformation wear factors, ϕ and ε, were determined based on the assumptions that for the materials with high hardness more energies of cutting wear and deformation wear are required to remove the target material during an erosion process, and for high strength alloys large values of ϕ and ε are required. These assumptions indicate that hardness and strength may exhibit some intrinsic correspondences to ϕ and ε values. Based on such correlations, a parametric method was applied to obtain ϕ and ε for various alloys with the assistance of material properties of these alloys such as hardness, yield strength and tensile strength. The calculated values of ϕ_{NiAl} and ε_{NiAL}, along with other parameters that are required by (16) and (17) are listed in Table III. For the κ value (velocity component normal to the surface below which no erosion takes place) in the equations, as suggested by [6]; for metals it is often the case that κ is neglected because the cutting wear predominates and the κ value is usually very small compared to the particle velocity. The constant n in the equations was taken as 5, according to the test conducted by [6].

TABLE III
Parameters of Aluminum-Nickel Alloy for Oxide Thickness Computation

Parameter	Value
a (M_aO_b, Al_2O_3)	2
b (M_aO_b, Al_2O_3)	3
V_m (molar volume of the alloy)	1.242×10^{-5} (m^3/mol)
M_o (Atomic weight of oxygen)	0.016 (kg/mol)
d (density of particle)	2700 (kg/m^3)
ϕ (cutting wear factor)	3.3939×10^7 (N·m/kg)
ε (deformation wear factor)	7.5034×10^7 (N·m/kg)

The material properties of the liquid and NiAl alloy used in the liquid-drop erosion model are given in Table IV. The minimum target thickness to avoid the occurrence of damage was computed with increasing the drop size using (21). The c_L and c_S values were calculated from (22) and (23).

TABLE IV
Parameters of Aluminum-Nickel Alloy and Liquid for Erosion Maps

κ - bulk modulus of NiAl	230 GPa
E - Young's modulus of NiAl	250 GPa
G - shear modulus of NiAl	94 GPa
K_{IC} - fracture toughness of NiAl	25×10^6 Pa.m$^{1/2}$
ρ - density of NiAl	7.8×10^3 kg/m^3
H - hardness of NiAl	180 HB
ρ_0 - density of liquid	10^3 kg/m^3
κ_0 - bulk modulus of liquid	2.2 GPa

The MDRP of eroded NiAl surface was computed against the velocity of liquid droplet using (30). It is suggested that erosion strength parameter S_c is approximately proportional to the hardness of target surface material [17]. Therefore for the S_c value of NiAl alloy, the experimental measurement on pure Al to obtain it S_c value in the previous research by Hattori [17]

was utilized. Using (20) and (32) to obtain the C_R and C_w values for NiAl alloy with the material properties in Table IV and substituting these values together with other material properties in Table IV into (31), the DTV was computed with varying drop size.

B. Results of NiAl Alloy from Models

The computations were implemented using Matlab computer program. The variations of the oxide scale thickness with erosion time of NiAl alloy under high-temperature erosion were computed for different erosion conditions and the results are plotted in Figs. 4-7. As shown in Fig. 4, at high temperatures without particle impact, oxide growth rates are appreciable and proportional to expose time, and also the growth rate of oxide thickness is proportional to temperature. At 950℃, the oxide thickness increases to 0.1012 μm from original value of 0.1 μm at the time $t = 0$ s within 60 s. At 900℃, the oxide thickness reaches 0.1009 μm, and at 850℃, the oxide thickness reaches 0.1004 μm. The thickness growth rate at 950℃ is about 3 times higher than the rate at 850℃, and 1.5 times the rate at 900℃.

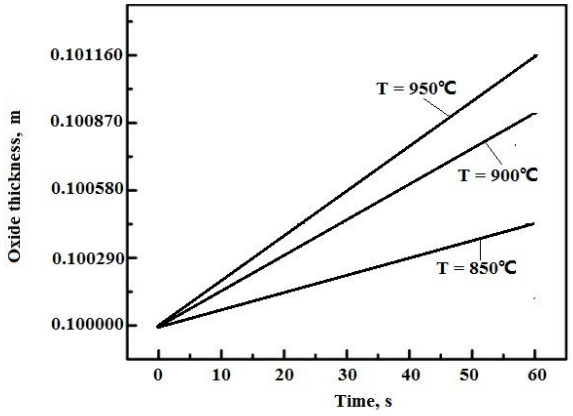

Fig. 4 Variations of oxide scale thickness with time for NiAl alloy without particle impact

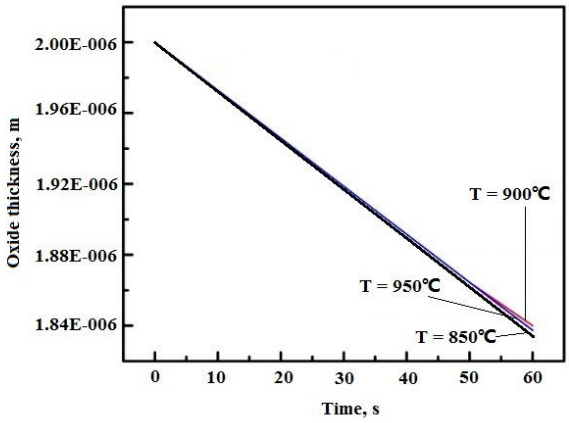

Fig. 5 Variations of oxide scale thickness with time for NiAl alloy under erosion at particle impact velocity of 10 m/s and particle impact angle of 15 degree

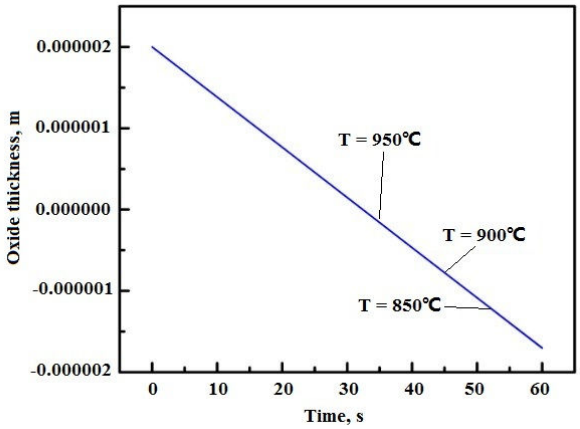

Fig. 6 Variations of oxide scale thickness with time for NiAl alloy under erosion at particle impact velocity of 50 m/s and particle impact angle of 90 degree

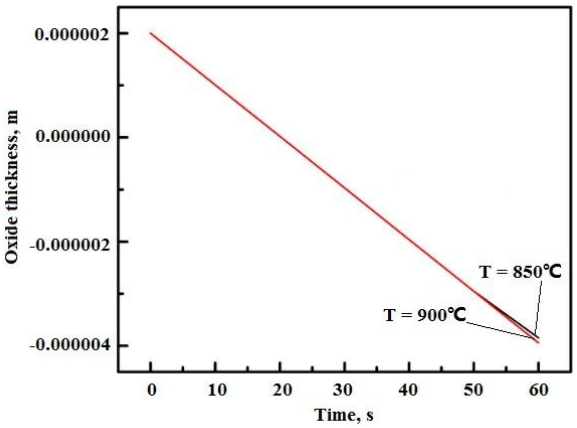

Fig. 7 Variations of oxide scale thickness with time for NiAl alloy under erosion at particle impact velocity of 50 m/s and particle impact angle of 45 degree

The computational results of liquid-drop erosion for NiAl alloy are plotted in Figs. 8-10. It is shown that the minimum target thickness for avoiding erosion damage increases linearly with drop size (diameter), see Fig. 8. The increase of required target thickness with larger drop size can be explained as the bigger the droplet, the larger the contact area is and also the heavier the impact of drop is, thus the more severe the attack of erosion is. For the MDRP of NiAl alloy, as shown in Fig. 9, the MDRP is trivial at very low drop velocities (< 200 m/s), but it increases steadily with drop velocity between 200 m/s and 400 m/s, and then rises rapidly at high drop velocities. Doubtlessly, drop velocity has significant influence on the MDRP, which is parametrically related to erosion resistance.

In regard of the DTV, it decreases with drop size, as seen in Fig. 10. Within the range of drop size 50 to 100 μm, which is common in reality, the corresponding DTV is very high and above 1000 m/s. Therefore, in practice, if the drop velocity is less than 1000 m/s, erosion damage would not occur on NiAl alloy.

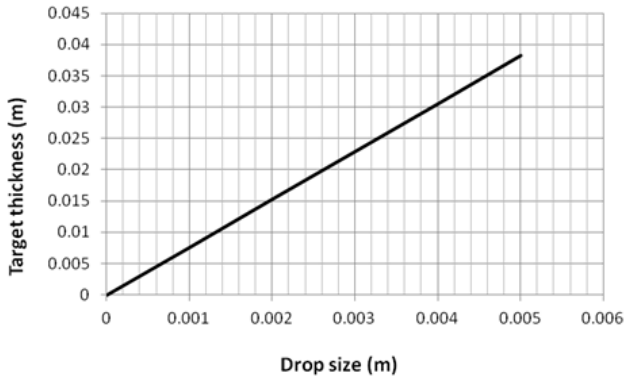

Fig. 8 Target thickness ~ drop size map of NiAl alloy

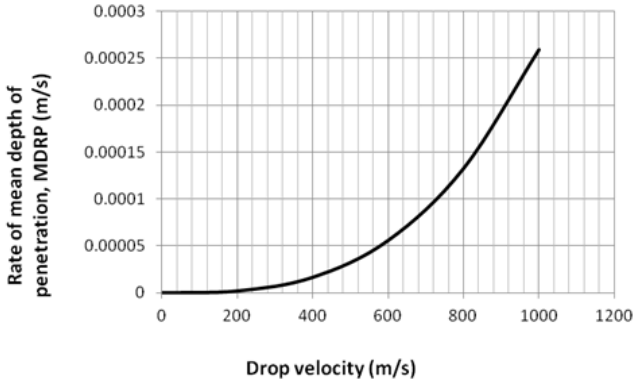

Fig. 9 MDRP ~ drop impact velocity map of NiAl alloy

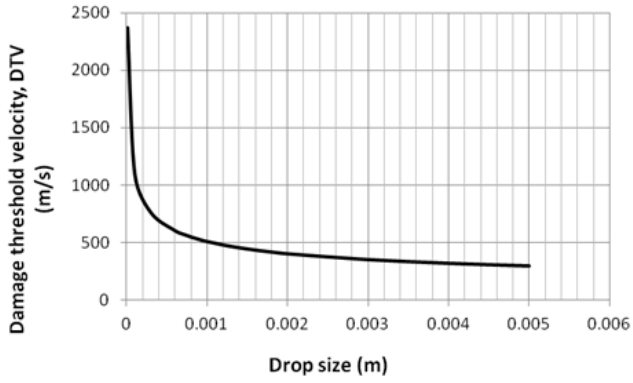

Fig. 10 DTV ~ drop size map of NiAl alloy

V. Discussion

Without erosion attack, the oxide thickness on NiAl alloy surface increases with temperature. This is because oxidation is promoted by temperature. However, it is observed that the growth rate of the oxide on NiAl alloy is very low due to the limited Al content, compared with that on pure Al [29]. In addition, the trend of the oxide thickness growth is actually parabolic; however, because the time interval is only 60 s and the value of parabolic constant K_p is small, the plotted curves exhibit a shape close to straight line.

When particles impact the NiAl alloy surface that has an oxide scale of 2 μm, at a velocity of 10 m/s and at an impinging angle of 15 degree, the thickness of the oxide is reduced from initial 2 μm to 1.84 μm in 60 s, as shown Fig. 5. In other words, when erosion is involved, the oxide thickness decreases with time. It can be deducted that after a certain period of time, the oxide thickness will become zero. In this case, the substrate material will be eroded and oxidation will not benefit preventing erosion degradation, that is, erosion is the type of regime 2 — oxidation-affected erosion.

Furthermore, when the particle impact velocity is raised, the frequency of particle impact on the target surface is increased; then the oxide removal from the surface is expedited. As illustrated in Fig. 6, within 60 s at the particle impact velocity of 50 m/s, the oxide thickness becomes negative, that is, no oxide is on the surface at all. Also, at the same particle impact velocity of 50 m/s, the smaller impinging angle causes larger oxide removal. This can be seen by comparing the curves in Fig. 6 with those in Fig. 7. This indicates that for ductile materials (metals), cutting wear predominates in erosion, which has been proved by previous research [6], [30].

Moreover, from Figs. 5-7, it is observed that at the particle impact velocities of 10 m/s and 50 m/s, the temperature almost does not affect the oxide thickness; in particular, at the higher velocity the oxide thickness does not vary with temperature, as seen in Figs. 6 and 7. The reason for this is that the oxide growth rate of this alloy is very low, therefore at high particle impact velocities there is no enough time in the interval between impacts for oxide to form.

From Figs. 9 and 10, it is clear that in liquid-drop erosion when drop velocity is very low (< 200 m/s) and droplet is very small (< 10 μm), erosion damage would nearly not occur on NiAl alloy. However, the increasing rate of MDRP for this alloy is raised by drop velocity increase, which can be described by the derivative of the MDRP equation. On the other hand, the decreasing rate of DTV is reduced by drop size increase, which can be demonstrated by the derivative of the DTV equation. This may be explained by the cavitation damage mechanism, which is activated when a sufficient liquid volume exists at the solid/water interface, in addition to the drop kinetic energy.

VI. Conclusions

The variation of the oxide thickness with erosion time can reveal the damage behavior of the eroded surface. Due to the low growth rate of the oxide, the oxide thickness decreases with erosion time for NiAl alloy under high-temperature erosion, which indicates that oxidation does not play a significant role in contribution to erosion resistance of this alloy.

The oxide thickness results show that the erosion damage at the smaller particle impinging angle is larger, which confirms that cutting wear predominates the erosion of this alloy, which is ductile.

The minimum target thickness (m) for NiAl alloy to avoid erosion damage is increased with drop diameter (m) by a factor of 7.63. The higher the drop velocity, the larger the rate of mean depth of penetration is, and the greater the drop diameter, the lower damage threshold velocity is. The rate of mean depth of penetration increases rapidly with high drop velocities. Within

the range of drop size 50 to 100 μm, the damage threshold velocity for this alloy is above 1000 m/s.

ACKNOWLEDGMENT

The authors are grateful for financial support from the Natural Science & Engineering Research Council of Canada (NSERC), in-kind support form National Research Council Canada, and both financial and in-kind support of Kennametal Stellite Inc.

REFERENCES

[1] P. J. Blau, *Friction and Wear Transitions of Materials*. Noyes Publications: Park Ridge, 1989.
[2] G. S. Springer, *Erosion by Liquid Impact*. John Wiley & Sons Inc.: Washington D.C., 1976.
[3] I. Finnie, "Erosion of surfaces by solid particles," *Wear*, vol. 3, pp. 87-103, 1960.
[4] J. G. A. Bitter, "A study of erosion phenomena, Part I," *Wear*, vol. 6, no. 1, pp. 5-21, 1963.
[5] J. G. A. Bitter, "A study of erosion phenomena, Part II," *Wear*, vol. 6, no. 3, pp. 169-190, 1963.
[6] J. H. Neilson and A. Gilchrist, "Erosion by a stream of solid particles," *Wear*, vol. 11, no. 2, pp. 111-122, 1968.
[7] G. Sundararajan, "An analysis of the erosion-oxidation interaction mechanisms," *Wear*, vol. 145, no. 2, pp. 251–282, 1991.
[8] S. Hogmark, A. Hammersten, and S. Soderberg, "On the combined effects of corrosion and erosion," in *Proc. 6th Int. Conf. on Erosion by Liquid and Solid Impact*, Cambridge, 1983, pp. 37.1–37.8.
[9] C. T. Kang, F. S. Pettit, and N. Birks, "Mechanisms in the simultaneous erosion-oxidation attack of nickel and cobalt at high temperature," *Metall. Trans. A*, vol. 18, no. 10, pp. 1785-1803, 1987.
[10] M. M. Stack and L. Bray, "Interpretation of wastage mechanisms of materials exposed to elevated temperature erosion-corrosion using erosion-corrosion maps and computer graphics," *Wear*, vol. 186–187, no. 1, pp. 273–283, 1995.
[11] D. M. Rishel, F. S. Pettit, and N. Birks, "Some principal mechanisms in the simultaneous erosion and corrosion attack of metals at high temperature," in *Proc. Conf. Corrosion-Erosion-Wear of Materials at Elevated Temperatures*, Houston, 1990, pp. 1-23.
[12] E. Honegger, "Corrosion and erosion of steam turbine blading," *Brown Boveri Rev.*, vol. 12, pp. 263-278, 1924.
[13] M. A. Cook, R. T. Keyes, and W. O. Ursenbach, "Measurements of detonation pressure," *J. Appl. Phys.*, vol. 33, pp. 3413-3411, 1962.
[14] O. G. Engel, "Fragmentation of waterdrops in the zone behind an air shock," *J. Res. Nat'l Bur. Stand.*, vol. 60, no. 3, pp. 245-280, 1958.
[15] G. Hoff, G. Langbein, and H. Rieger, "Erosion by Cavitation or Impingement," *ASTM STP*, vol. 408, 1967, pp. 42-69.
[16] D. W. C. Baker, K. H. Jolliffe, and D. Pearson, "The resistance of materials to impact erosion damage," *Philos. Trans. R. Soc. Lond. A*, vol. 260, pp. 193-203, 1966.
[17] S. Hattori, "Effects of impact velocity and droplet size on liquid impingement erosion," in *Proc. International Symposium on the Ageing Management & Maintenance of Nuclear Power Plants*, 2010, pp. 58-71.
[18] W. F. Adler and T. W. James, "Analysis of water impacts on zinc sulfide," in *Fracture Mechanics of Ceramics*. Plenum Press: New York, 1983, pp. 27-46.
[19] J. V. Hackworth, "Damage of infrared-transparent materials exposed to rain environments at high velocities," in *Proc. of SPIE*, vol. 362, 1982, pp. 123-136.
[20] R. J. Hand and J. E. Field, "Liquid impact on toughened glasses," *Eng. Fract. Mech.*, vol. 37, pp. 293-311, 1990.
[21] A. G. Evans, M. E. Gulden, G. E. Eggum, and M. Rosenblatt, "Impact damage in brittle materials in the plastic response regime," *Report No. SC5023*, Rockwell International Science Center, 1976.
[22] P. Carter, B. Gleeson, and D. J. Young, "Calculation of precipitate dissolution zone kinetics in oxidizing binary two phase alloys," *Acta Materialia*, vol. 44, no. 10, pp. 4033–4038, 1996.
[23] F. J. Heymann, "A survey of clues to the relation between erosion rate and impact parameters," in *Proc. of the 2nd International Conference Rain Erosion*, 1967, pp. 683-760.
[24] L. E. Kinsler, A. R. Frey, A. B. Coppens, and J. V. Sanders, "Transverse motion: The vibrating string," in *Fundamentals of Acoustics*, John Wiley and Sons Inc.: New York, 2000, pp. 37-51.
[25] P. R. K. Padmini and B. R. Rao, "Molar sound velocity in molten hydrated salts," *Nature*, vol. 191, pp. 694 – 695, 1961.
[26] J. Krautkrämer and H. Krautkrämer, *Ultrasonic Testing of Materials*. Springer-Verlag, Berlin Heidelberg: New York, 1990, pp. 251-255.
[27] O. Gohardani, "Impact of erosion testing aspects on current and future flight conditions", *Progress in Aerospace Sciences*, vol. 47, pp. 280–303, 2011.
[28] L. Nalin, "Degradation of Environmental Protection Coatings for Gas Turbine Materials," Ph.D. Thesis, Cranfield University, UK, 2008.
[29] V. Pankcov, L. Zhao, "Durability Testing of a Thin Film Thermocouple Sensor Fabricated by Pulsed Laser Deposition," *LTR-SMPL-2012-0081 Report*, National Research Council Canada, Ottawa, 2012.
[30] S. Nsoesie, R. Liu, K. Y. Chen, and M. X. Yao, "Analytical modeling of solid-particle erosion of Stellite alloys in combination with experimental investigation," *Wear*, vol. 309, no. 1-2, pp. 226-232, 2014.

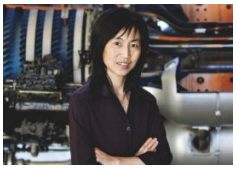

Rong Liu was born in China on August 25, 1962. She received a Bachelor degree of mechanical engineering from Northeastern University, Shenyang, Liaoning, China, in 1983; a Master degree of mechanical engineering from Northeastern University, Shenyang, Liaoning, China, in 1990; a Master degree of materials engineering from University of Wollongong, Wollongong, New South Wales, Australia, in 1995; a Ph.D. degree of mechanical engineering from Deakin University, Geelong, Victoria, Australia, in 1998.

She was a Mechanical Engineer of Shenyang Aluminum Magnesium Engineering and Research Institute, China, during 1983 to 1987 and 1990 to 1994. She was a Postdoctoral Fellow of the Department of Chemical and Materials Engineering, University of Alberta, Canada, during 1998 to 2000. She was an Assistant Professor of the Department of Mechanical and Aerospace Engineering, Carleton University, Canada, during 2000 to 2005. She was an Associate Professor of the Department of Mechanical and Aerospace Engineering, Carleton University, Canada, during 2005 to 2012. She was a Professor of the Department of Mechanical and Aerospace Engineering, Carleton University, Canada, from 2012 until now. Published book chapter: Chapter 4 High-Temperature Wear/Corrosion Resistant Stellite Alloys and Tribaloy Alloys, in *CRC Handbook on Aerospace and Aeronautical Materials*, CRC Press, Taylor & Francis, July 2012. Published article: Analytical modeling of solid-particle erosion of Stellite alloys in combination with experimental investigation, *Wear,* vol. 309, no. 1-2, pp. 226-232, 2014. Published article: A fracture toughness model for brittle coating on ductile substrate under indentation loading, *Engineering Fracture Mechanics*, vol. 82, pp. 17-28, 2012. Her research interests include fracture mechanics of high-temperature materials; erosion and corrosion of superalloys; surface coatings; finite element analysis.

Professor Liu is a member of the American Society for Metals (ASM) and a member of the Professional Engineers of Ontario (PEO), Canada. Professor Liu was awarded by Carleton University Research Works in 2009.